

Article

High Specific Capacitance of Polyaniline/Mesoporous Manganese Dioxide Composite Using KI-H₂SO₄ Electrolyte

Zhongkai Hu ^{1,2}, Lei Zu ^{1,2}, Yanhua Jiang ¹, Huiqin Lian ¹, Yang Liu ¹, Zhenzi Li ³, Fei Chen ^{3,*}, Xiaodong Wang ² and Xiuguo Cui ^{1,*}

Received: 19 July 2015 ; Accepted: 14 September 2015 ; Published: 30 September 2015

Academic Editor: Hsing-Lin Wang

¹ Beijing Key Laboratory of Specialty Elastomer Composite Materials, Beijing Institute of Petrochemical Technology, Beijing 102617, China; huzhongkai@bipt.edu.cn (Z.H.); jiangyanhua@bipt.edu.cn (Y.J.); lianhuiqin@bipt.edu.cn (H.L.); yang.liu@bipt.edu.cn (Y.L.)

² State Key Laboratory of Organic-Inorganic Composites, Beijing University of Chemical Technology, Beijing 100029, China; zulei@mail.buct.edu.cn (L.Z.); wangxd@mail.buct.edu.cn (X.W.)

³ College of Materials Science & Engineering, Beijing Institute of Petrochemical Technology, Beijing 102617, China; m13811097980@163.com

* Correspondence: cuixiuguo@bipt.edu.cn (X.C.); chenfei@bipt.edu.cn (F.C.);
Tel./Fax: +86-10-8129-4007 (X.C.)

Abstract: The PANI/Mesoporous MnO₂ composites were prepared through a simple one step method and we introduced the KI-H₂SO₄ solution as the electrolyte of PANI/MnO₂ composites creatively. The characterization of structure, morphology, and composition are obtained by X-ray diffraction, Fourier transform infrared spectroscopy, thermal gravity analysis, Raman spectra, and scanning electron microscope. The electrochemical performances were investigated by constant-current charge–discharge, the voltammetry curve, and alternating current (AC) impedance technique. The specific capacitance of composites is 1405 F/g, which is almost 10 times larger than MnO₂ (158 F/g). We also find that the iodide concentration is closely related to the specific capacitance. Therefore, we explored the specific capacitance at different iodide concentration (0.05, 0.1, 0.2, 0.5, and 1 M), the results indicated that the specific capacitance reached a maximum value (1580 F/g) at 0.5 mol/L. Additionally, the PANI/Mesoporous MnO₂ composites not only exhibited a good ratio discharge property (857 F/g) at high current density, but also revealed an excellent cycling stability after 500 cycles, which retained 90% of the original specific capacitance.

Keywords: polyaniline; mesoporous MnO₂; specific capacitance; KI

1. Introduction

Nowadays, with the development of science and technology, mankind has become an information society. The popularity of computer, mobile communications equipment, and other electronic equipment are crying out for a high-performance energy storage device. As commonly used for maintaining power, there are defects in batteries and electrostatic capacitors' application [1–3]. Even though the electrostatic capacitors have high power density, nevertheless, its energy storage is low. The batteries are obviously insufficient in service life. Therefore, super-capacitors, as a high-performance energy storage device, have been attracting significant attentions lately due to their wide range of applications in hybrid electric vehicles, information technology, aerospace, etc. Electrode materials are the key factor of super-capacitor's capacitance performance. Metal oxides [4], conducting polymers [5], and carbon porous nanoparticles [6] have been identified as the most

promising materials for super-capacitors, whose modification and compounds are being used to enhance the material performance [7–10].

To date, the capacitance in an electrochemical capacitor can arise from electrical double layer and pseudocapacitance on the charge storage mechanisms [11,12]. The pseudocapacitance materials include not only traditional polymer and transition metal oxide [13,14], but also the emerging metal chalcogenides [15,16] and binary metal oxides [17,18]. Large numbers of researchers have applied the nanocomposites of conducting polymers and metal oxides to energy storage [19,20]. Among the metal oxides, hydrous RuO_2 , NiO , CoO_x , and V_2O_5 have been researched and implemented as electrode material [21–24]. However, the low capacitance and high cost limits their range of applications and have motivated the research into other transition metal oxides. MnO_2 has been regarded as an ideal candidate due to its affordable and easily prepared advantages [25,26]. Conducting polymers are a promising electrode material due to their faster doped/doping mechanisms [27–29]. The polyaniline (PANI) could act as an active electrode material for a super-capacitor because of controllable electrical conductivity, high environmental stability, and capacitance performance [30–32]. Even though the theoretical specific capacitance of separate manganese dioxide can reach 1370 F/g [33], whereas the practical specific capacitance still keeps several hundred farads which need to be improved by researchers. The PANI also has higher specific capacitance, but the poor mechanical property seriously limits its practical applications.

In recent years, considerable efforts have been carried out to couple the unique advantages of PANI and MnO_2 . The research of PANI/ MnO_2 has been the heated topics in many scientific establishments. Sun *et al.* fabricated PANI/ MnO_2 composites (532 F/g) by exchange reaction of polyaniline and MnO_2 in *N*-methyl-2-pyrrolidone solvent, which was tested in 0.1 M NaNO_3 solution [34]. Liang *et al.* obtained the PANI/ MnO_2 composites with the method of electroplating, the specific capacitance just reaches 80 F/g in 0.5 M H_2SO_4 and 0.6 M $(\text{NaPO}_3)_6$ electrolyte [35]. All kinds of PANI/ MnO_2 have been synthesized or modified by other materials. Nevertheless, the specific capacitance of the overwhelming majority of research are generally several hundred Farad per gram [36–39]. Therefore, it is necessary to find a breakthrough point to improve the specific capacitance.

Adding the redox additive to electrolyte is an emerging pattern to enhance the electrochemical performance, which has been applied by Su *et al.* using $\text{Fe}(\text{CN})_6^{3-}/\text{Fe}(\text{CN})_6^{4-}$ ions as an additive [40]. The specific capacitance was increased from 226 to 712 F/g. The oxidation-reduction reaction of the additive generates additional electrons, enhancing the pseudocapacitance. VO^{2+} , Cu^{2+} , Fe^{2+} , and I^- are effective candidates in applications [41–43]. However, these ions are only widely applied to asymmetric electrode, which are constructed by assembling two round electrodes with a membrane between them. There are few applications in mixed electrolyte which are simple and efficient. Iodine has a variety of valences; there are a number of reversible oxidation-reduction reactions between different valence state iodine [44]. Therefore, I_2 has been used to dope polyaniline by many researchers, whereas they just studied the electrical conductivity [45] and few researchers researched the effects to specific capacitance. Additionally, during the process of the protonation of PANI, the H^+ combined with the PANI molecular chain, thus making the molecular chain carry a positive electric charge, I^- , I_3^- , or I_5^- will attach to the molecular chain immediately to keep electric neutrality [46,47]. There are some electrochemical reactions among I^- , I_3^- , and I_5^- , these will have a positive impact on electrochemical performance. From the above, I^- can be feasibly and effectively applied in increasing the specific capacitance of PANI than other materials.

In this work, we synthesized high specific surface area mesoporous MnO_2 , which is applied to catalyze aniline and composite with PANI. KI was innovatively introduced to the electrolyte to increase the electrochemical performance. As far as we know, there are no other researchers using KI- H_2SO_4 solution as electrolyte for PANI/ MnO_2 composites. We also explored the specific capacitance under the 0.05, 0.1, 0.2, 0.5, and 1 M KI-1 M H_2SO_4 solution. We not only obtained high

specific capacitance through KI-H₂SO₄ electrolyte, but also found the most effective concentration of I[−] to function.

2. Experimental Section

2.1. Chemicals

Potassium permanganate (KMnO₄, Aladdin, Shanghai, China), ethylene glycol (C₂H₆O₂, Aladdin, Shanghai, China), sulfuric acid (H₂SO₄, Aladdin, Shanghai, China), hydrochloric acid (HCl, Aladdin, Shanghai, China), aniline (AN, Aladdin, Shanghai, China), acetylene black, polyvinylidene fluoride (PVDF, Aladdin, Shanghai, China), 1-methyl-2-pyrrolidinone (NMP, Aladdin, Shanghai, China) were utilized. The aniline was purified by vacuum distillation in advance.

2.2. Synthesis

2.2.1. Mesoporous Manganese Dioxide Preparation

In a typical synthesis of MnO₂, 4 g KMnO₄ were dissolved in 100 mL distilled water by stirring at room temperature for 30 min. At the same time, 4 mL ethylene glycol was added to 8 mL H₂SO₄ while continuously stirring until a homogeneous solution is formed. Then, the homogeneous solution was poured into the previous KMnO₄ solution by stirring for additional 30 min. The brown precipitate was repeatedly washed with water until the PH of filtrate is approaching to neutral.

2.2.2. Polyaniline/Mesoporous Manganese Dioxide Composites Preparation

Two gram of MnO₂ is mixed with 1.5 mol/L HCL solution under the agitation condition for 5 min and then 1.5 g AN monomer was added into the mixture solution. An hour later, the composites are collected and washed with water several times and then air-dried at 60 °C for an additional 48 h.

2.3. Characterization

Scanning electron microscopy (SEM) observations were carried out in a COXEM-20 microscope (COXEM, Daejeon, Korea) at 20 kV. Infrared spectrometry (IR) analyses were performed on a Thermal Nicolet infrared spectrometer (Thermo Fisher Scientific Inc., Waltham, MA, USA). Thermogravimetric analyses (TGA) were performed using a TA instruments TGA 2050 (Waltham, MA, USA) from room temperature to 600 °C, with a heating rate of 10 °C min^{−1} under nitrogen. Wide angle X-ray diffraction (WAXD) patterns were obtained with a Bruker D8 diffractometer (BRUKER AXS, Berlin, Germany) in reflection mode using Cu Kα = 0.154 nm with a voltage of 40 kV, the Raman spectra were carried out using Raman spectrometry (RENISHAW in Via Raman Microscope, London, UK).

2.4. Preparation of Electrodes and Electrochemical Characterization

The working electrode was prepared by mixing active materials, acetylene black, and polyvinylidene fluoride (PVDF) in NMP with a mass ratio of 8:1:1 and then dried at 70 °C under vacuum for 12 h. The mass of the active material is controlled in 5 mg, and the substrate is a stainless steel sheet that the length is 8 cm and the width is 1 cm. The area loading the active materials is 1 cm² (1 cm × 1 cm). The electrochemical measurements were performed by a standard three-electrode cell. A saturated calomel electrode (SCE) was used as the reference electrode and a Pt foil electrode (about 1 cm²) was used as the counter electrode. The electrolyte was composed of 1 M H₂SO₄ and 1, 0.5, 0.2, 0.1, 0.05 M KI. The cyclic voltammetry (CV) tests were carried out between −0.3 and 0.7 V (*vs.* SCE) at a scan rates of 5, 10, 20, 50, and 100 mV·s^{−1}. The galvanostatic charge/discharge analyses were accomplished in the potential range of 0–0.35 V (*vs.* SCE) at 0.5, 1, and 2 A·g^{−1}.

3. Results and Discussion

3.1. SEM Analysis

The morphologies of the MnO_2 and PANI/ MnO_2 composite were investigated by SEM. Figure 1a reveals that large numbers of manganese dioxide particles are evenly distributed. As is shown in Figure 1b, the PANI/ MnO_2 composites still keep the similar graininess, even though some particles agglomerate together. The surface of the composites is very smooth, but not as coarse as the study of other researchers [35]. For the catalysis of MnO_2 to aniline, the PANI is synthesized on the surface of MnO_2 and the MnO_2 may be well wrapped inside by PANI. According to these results, we can infer that the good contact between PANI and MnO_2 is conducive to the transfer of electrons, enhancing the specific capacitance.

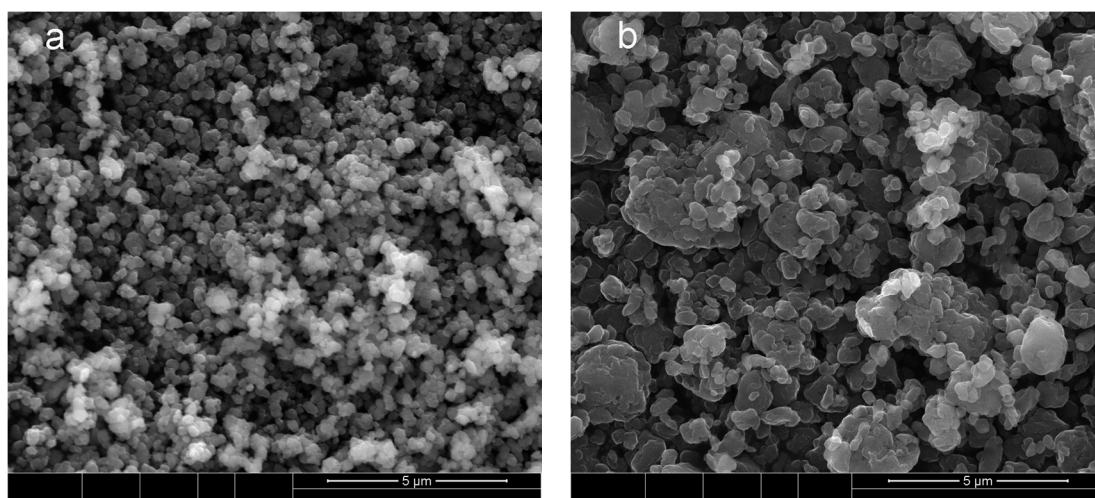


Figure 1. SEM of (a) mesoporous MnO_2 and (b) PANI/ mesoporous MnO_2 .

3.2. XRD and FTIR Analysis

To obtain more chemical composition and mechanics information of the composites, the XRD and FTIR spectra are shown in Figures 2 and 3. Figure 2 shows the XRD patterns of the PANI, MnO_2 , and PANI/ MnO_2 . There are two resolved peaks of MnO_2 in the XRD spectra at 2θ angle of 36.9° and 66.3° . The phase of MnO_2 is δ according to the Joint Committee on Powder Diffraction Standards (JCPDS) No.42-1317, the 36.9° is associated with (111), the 66.3° is relevant to (312) [48]. The low intensity of the bands of MnO_2 indicates the poor crystallinity of δ - MnO_2 , which has been reported by other researchers [49]. As is shown in Figure 2, the PANI/ MnO_2 exhibits ideal X-ray diffraction peak at 36.9° and 66.3° (corresponding to the pure MnO_2) [48], 14.4° , 19.6° , and 25.4° (corresponding to the pure PANI) [50]. However, the intensity of the peaks decreases slightly, which is due to the interaction between PANI and MnO_2 . The PANI attached to MnO_2 still keeps good crystallization, contributing to the electrical conductivity. The FTIR for MnO_2 , PANI, and PANI/ MnO_2 composites are displayed in Figure 3. The characteristic IR peaks of MnO_2 can be attributed to the stretching vibration peak of Mn–O (505 cm^{-1}) [51], which can be also observed in the PANI/ MnO_2 composites. The peaks appearing at 1297 and 1569 cm^{-1} correspond to the C–N and C=N bands. Additionally, the typical 1,4-substituted phenyl ring stretching is observed at 820 cm^{-1} [52], indicating the backbone structure indirectly. The characteristic absorption bands of PANI/ MnO_2 composites emerge in both MnO_2 and PANI, demonstrating the existence of both components in the composites.

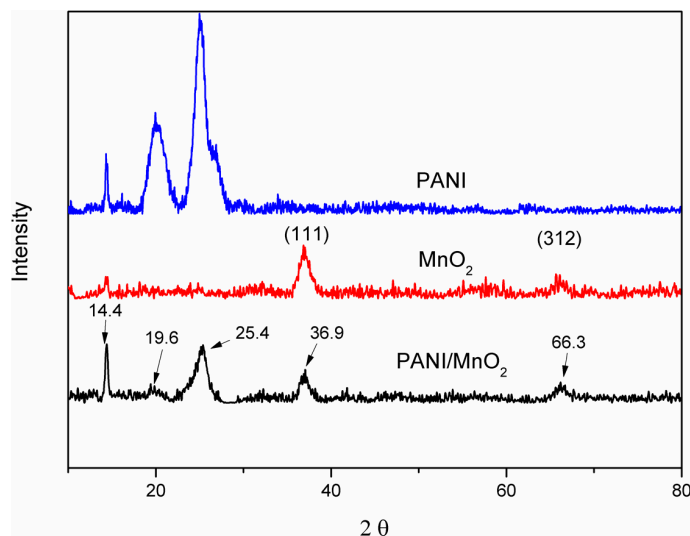


Figure 2. XRD patterns of PANI, MnO₂ and PANI/MnO₂.

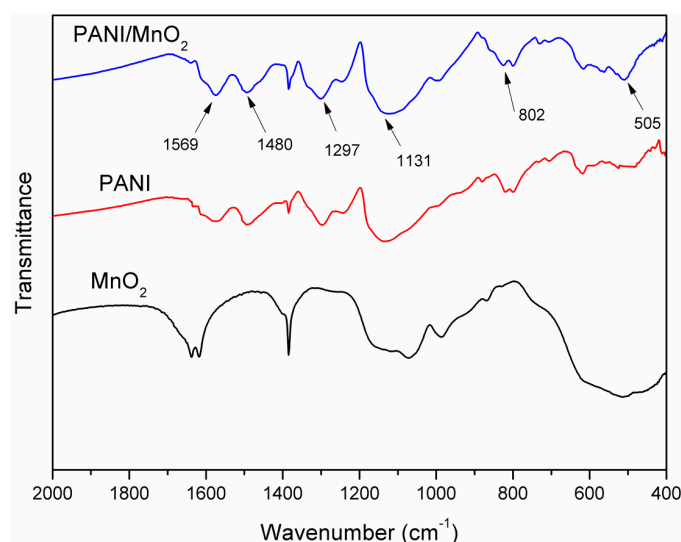


Figure 3. FT-IR spectra of PANI, MnO₂ and PANI/MnO₂.

3.3. TG and DTG Analysis

The thermal stability of MnO₂ and the PANI/MnO₂ composite were investigated by TG (Figure 4) and DTG (Figure 5). As is shown in Figure 4, The MnO₂ has a weight loss of 20% which is due to the removal of water existing both on the surface and in the lattice of the nanostructure before 250 °C [53]. The trace loss of MnO₂ between 500 and 700 °C is ascribed to the evolution of oxygen caused by the transformation from MnO₂ to Mn₂O₃ [54]. Figure 5 reveals that the PANI/MnO₂ possesses a typical four-step decomposition, which emerges a larger weightlessness that is mainly due to the decomposition of PANI between 500 and 700 °C [55,56]. The weightlessness still existed when the temperature was increased to 1000 °C, which is due to the carbonization of PANI under nitrogen atmosphere. There is almost 45% left, the residues are carbon and manganese oxide.

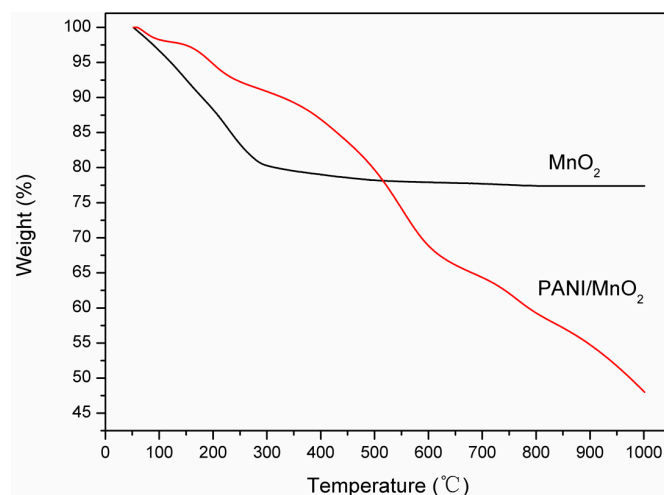


Figure 4. TG curves of MnO₂ and PANI/MnO₂.

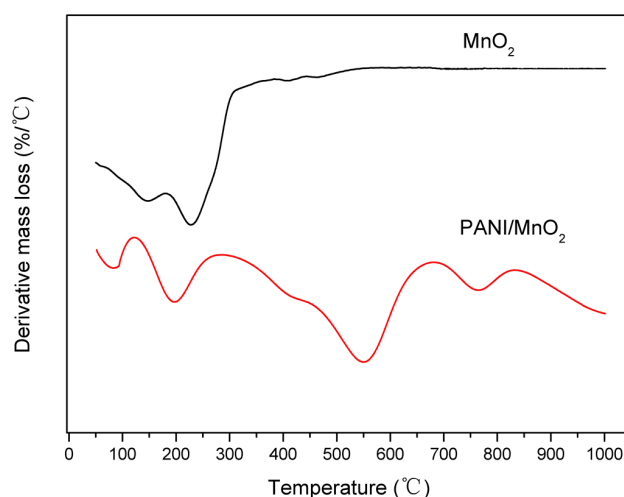


Figure 5. DTG curves of MnO₂ and PANI/MnO₂.

3.4. Electrochemical Properties Analysis

Figure 6a shows the CV curves of the PANI/mesoporous MnO₂ and MnO₂ measured at a scan rate of 5 mV/s in 1 mol/L H₂SO₄ and 0.2 mol/L KI solution in the potential range of −0.3 and 0.7 V. The PANI/mesoporous MnO₂ covers more current area than MnO₂ due to: (1) the inter-molecule between PANI and MnO₂ contact well; and (2) the PANI attached on the surface of MnO₂ is involved in oxidation-reduction reactions between different valence states of iodine ions [54,57]. During the process of polyaniline protonation, the molecular chain is positively charged due to the H⁺ attached to molecular chain. In order to maintain electric neutrality, the I[−] combined with polyaniline molecular chain where reversible redox reactions occurred, the schematic diagram is shown in Figure 7 [58–60]. The CV curve of PANI/MnO₂ shows a pairs of oxide and reduced peaks at 0.03 and 0.4 V, which is owing to the comprehensive results of the process of doped and doping PANI and possible oxidation-reduction reactions between 3I[−]/I₃[−] and 5I[−]/I₅[−].

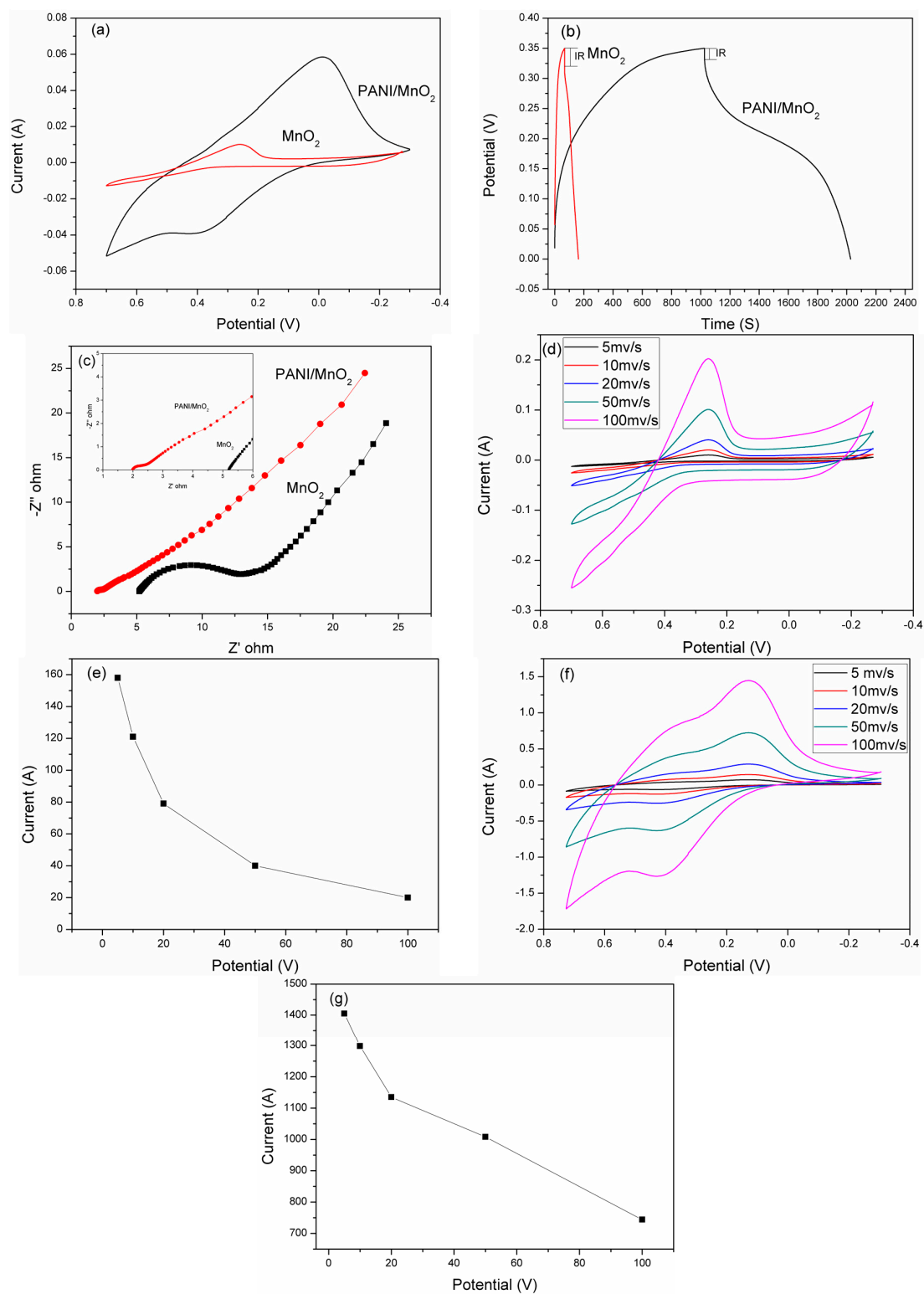


Figure 6. (a) CV curves of MnO₂ and PANI/MnO₂; (b) galvanostatic charge–discharge curve of PANI/MnO₂; (c) AC impedance curve of MnO₂ and PANI/MnO₂; (d) CV curves of PANI/MnO₂ at different scan rates in 0.2 M KI–1 M H₂SO₄; (e) Specific capacitances of the PANI/MnO₂ at different scan rates; (f) CV curves of MnO₂ at different scan rates in 0.2 M KI–1 M H₂SO₄; (g) Specific capacitances of the MnO₂ at different scan rates.

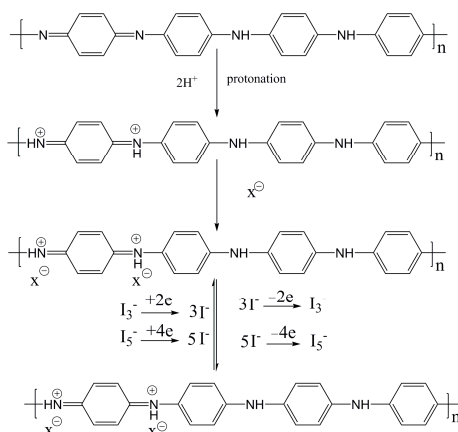


Figure 7. Schematic diagram of oxidation-reduction reactions among iodine with different valence. The x represents I^- , I_3^- , I_5^- , SO_4^{2-} , etc.

As shown in Figure 6b, the galvanostatic charge–discharge curve of PANI/ mesoporous MnO_2 was tested at a current density of 0.5 A/g. The linear variation of the voltage with time is observed, the longer the time is, the bigger of the specific capacitance is [61]. It can be obviously observed that the discharge time of PANI/mesoporous MnO_2 is larger than that under the MnO_2 charge–discharge curve. The specific capacitances of the MnO_2 and PANI/mesoporous MnO_2 calculated from the discharge time are 158 and 1405 F/g, respectively, which are similar to the calculated value of CV. The specific capacitance is calculated according to the Equations (1) and (2) [62]:

$$C_s = \frac{I\Delta t}{\Delta Vm} \tag{1}$$

where I is the current loaded (A), Δt is the discharge time (s), ΔV is the potential window during the discharge process, and m is the mass of active material in a single electrode (g).

$$C_s = \frac{\int IdV}{2M\Delta Vv} \tag{2}$$

where C_s is the specific capacitance in F/g, $\int idV$ is the integrated area of the CV curve, M is the mass of the active materials in the single electrode in g, ΔV is the potential window in V, and v is the scan rate (v/s).

Additionally, both the discharge curves of MnO_2 and PANI/ MnO_2 have obvious voltage drops (IR). The IR drop of PANI/ MnO_2 is less than MnO_2 , demonstrating that the PANI/ MnO_2 composites have smaller internal resistance [63]. Figure 6c also reveals that the internal resistance of PANI/ MnO_2 and MnO_2 is 0.5 and 6 Ω , respectively, which is consistent with the charge–discharge curve. Low internal resistance is important for energy storage devices to improve the efficiency. As is shown in Table 1, the obtained specific capacitance is higher than the previous work of other researchers using different electrolyte. The higher capacitance is related to the electron gain or loss in the possible oxidation reduction reactions between the pairs of $3I^-/I_3^-$, $5I^-/I_5^-$, where occurred on the surface of electrode materials [42,64]. Therefore, the additional electrons gain and loss except for the PANI doped and doping in the electrolyte enhances the specific capacitance.

Figure 6d–g indicate the CV curves and specific capacitances of PANI/ MnO_2 and MnO_2 at different scan rates in 0.2 M KI–1 M H_2SO_4 . The specific capacitances of PANI/ MnO_2 and MnO_2 decreased with the increasing of the scan rate, the value of PANI/ MnO_2 is far greater than MnO_2 at the same scan rates. However, the specific capacitance of PANI/ MnO_2 still keeps 837 F/g at 100 mv/s, which is also larger than other reports in Table 1, revealing a good rate capability. The drop in the specific capacitance with the increasing of the scan rate may be related to two reasons: first, the scan

rate is so fast that the oxidation-reduction did not react fully in time; and second, at high scan rates, the ions diffuse into the micropore surface of active material difficultly and just infiltrate some large pores, thus leading to a decrease of active sites on the electrode surface [62].

Table 1. Comparison of specific capacitance of PANI/ Mesoporous MnO₂ with reported values.

Materials	Electrolytes	Test condition	Specific capacitance (F/g)	References
PANI/MnO ₂	1 M NaNO ₃ pH = 1	2.4 mA/cm ²	532	[34]
GE/PANI/MnO ₂	0.5 M Na ₂ SO ₄	0.5 A/g	755	[65]
PANI/MnO ₂	0.1 M Na ₂ SO ₄	1 A/g	330	[66]
PANI-ND-MnO ₂	0.5 M H ₂ SO ₄ , 0.6 M (NaPO ₃) ₆	1.67 mA/cm ²	415	[35]
PANI-PSSMA-MnO ₂	0.5 M Na ₂ SO ₄	100 uA/cm ²	556	[67]
PANI/MnO _x	1 M NaO ₃ pH = 1	1 mA/cm ²	588	[68]
PANI/MnO ₂	0.1 M Na ₂ SO ₄	5 mA/cm ²	715	[69]
PANI/MnO ₂	0.1 M Na ₂ SO ₄	50 mV/s	500	[70]
PANI/MnO ₂ /MWCNTS	0.5 M Na ₂ SO ₄ -H ₂ SO ₄	6.5 mA/cm ²	384	[71]
MnO ₂ /PANI/MWCNT	0.5 M Na ₂ SO ₄	20 mV/s	330	[38]
MnO ₂ /P(An-co-OAS)	1 M Na ₂ SO ₄	1 A/g	127	[51]
PANI/MnO ₂ /Carbon	0.1 M Na ₂ SO ₄	0.2 A/g	350	[72]
PANI/MnO ₂	0.1 M HClO ₄	50 mV/s	207	[73]
PANI/α-MnO ₂	1 M H ₂ SO ₄	2 A/g	626	[74]
PANI/MesoporousMnO ₂	0.5 M Na ₂ SO ₄	9 mA/cm ²	262	[39]
PANI/MesoporousMnO ₂	1 M H ₂ SO ₄ , 0.5 MKI	0.5 A/g	1580	Present work
		1 A/g	1142	
		2 A/g	857	

Furthermore, the electrochemical performances are also carried out in different concentrations of I⁻ ion. As is shown in Figure 8a, the CV curves show ideal reduction and oxidation peak at 0–0.2 V and 0.3–0.5 V. The CV curves show a larger area in 1 M H₂SO₄ + 0.5 M KI electrolyte than other concentrations, indicating the PANI/MnO₂ have better capacitive behavior at this concentration. The I⁻ have good conductivity and reversible oxidation-reduction, the large numbers of I⁻ contribute to more electrons [75]. Figure 8b reveals that the discharge time become short with the decreasing of I⁻. The specific capacitance calculated at the concentration of 1 mol/L, 0.5 mol/L, 0.2 mol/L, 0.1 mol/L, and 0.05 mol/L is 1374, 1580, 1405, 1010, and 571 F/g, respectively. The tendency is consistent with the CV curves that the specific capacitance is up to its maximum in 1 M H₂SO₄ + 0.5 M KI. Therefore, there may exist some inhibiting effect of electrochemical performance if I⁻ concentration is over the point. High-concentrated I⁻ may restrain the process of negative reaction to receive electrons, thus affecting the specific capacitance.

Figure 8c reveals the electrolyte resistance (R_s) calculated from the point of intersecting with the X-axis in the high-frequency range and the charge-transfer resistance (R_{ct}) calculated from the diameters of semicircle, which are shown in Table 2 [76,77]. The impedance data were modelled using an equivalent electrical circuit shown in Figure 9. As is can be seen from the Table 2, the R_s and R_{ct} decreased with the concentration of KI increases until the concentration up to 0.5 mol/L, the increasing of ions concentration not only enhanced the electrolyte conductance, resulting in the decrease of R_s , but can also provide more I⁻ to combine with the PANI causing the reversible oxidation-reduction reactions to occur more, leading to the increasing of the specific capacitance and the drop of R_{ct} . When the concentration is over 0.5 mol/L, the high concentration of I⁻ inhibited the reversible oxidation-reduction reaction, and it may cause the rise of R_s and R_{ct} indirectly. Overall, the composite has smaller R_s and R_{ct} in 1 M H₂SO₄ + 0.5 M KI electrolyte, which is beneficial to the ion migration and electron transport. The charging–discharging curves of PANI/MnO₂ at different current densities (1 M H₂SO₄ + 0.5 M KI electrolyte) are shown in Figure 8d; the specific capacitances decreases with the increasing of current density. The specific capacitance still manages to achieve 857 F/g at 2 A/g, exhibiting good high-rate discharge ability. The voltage window decreased compared with the CV, which may be due to the reason that I⁻ oxidation-reduction reactions may occur in a very narrow potential under constant current [42].

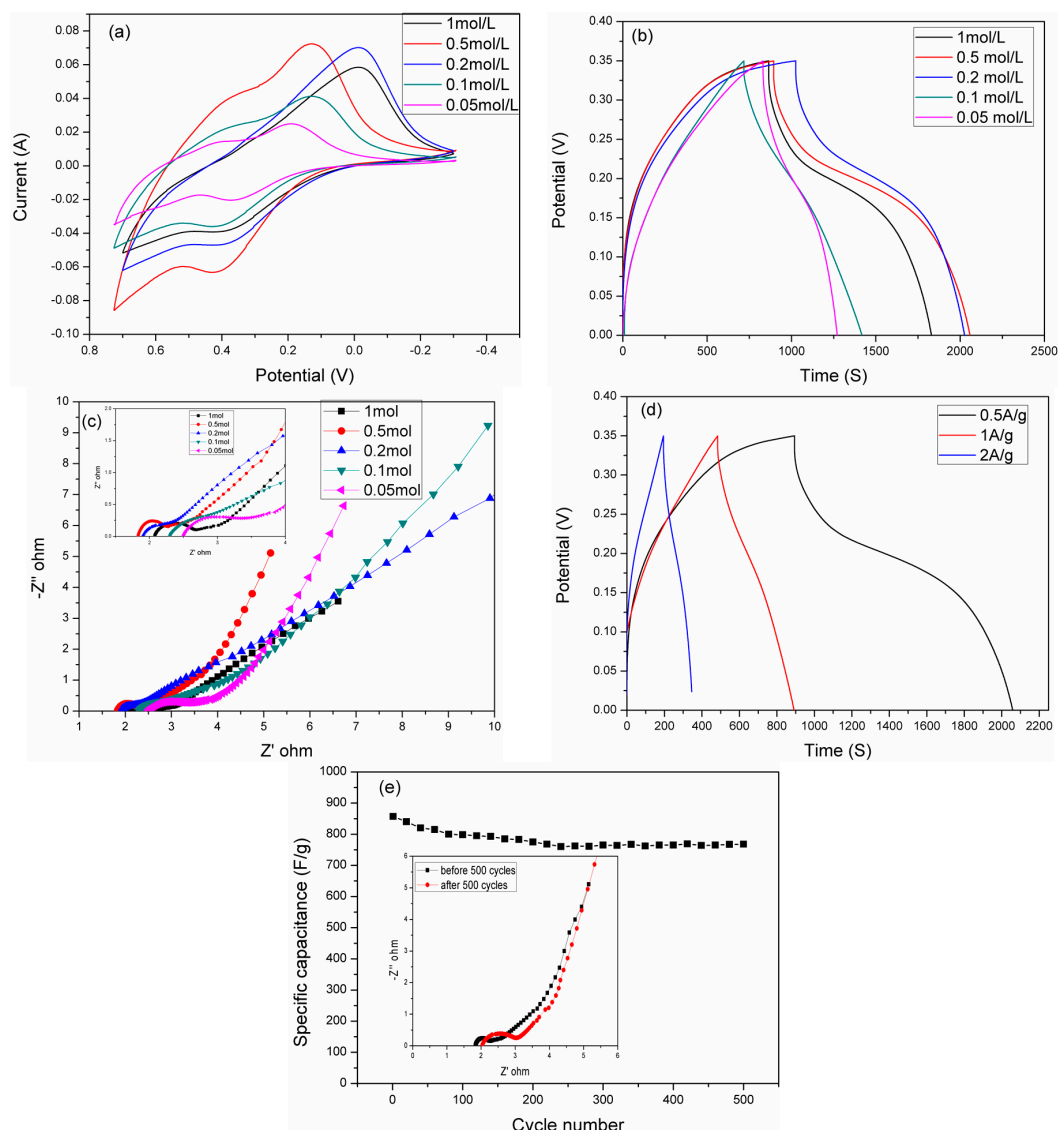
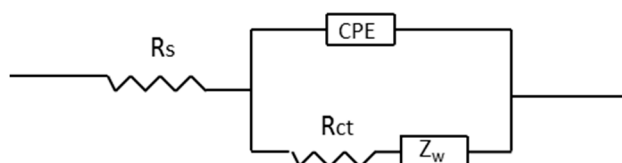


Figure 8. (a) CV curves of PANI/MnO₂ in different concentrations of KI with 1 M H₂SO₄ electrolytes; (b) galvanostatic charge–discharge curve of PANI/MnO₂ in different concentrations of KI with 1 M H₂SO₄ electrolytes; (c) AC impedance curve of PANI/MnO₂ in different concentrations of KI with 1 M H₂SO₄ electrolytes; (d) galvanostatic charge–discharge curve of PANI/MnO₂ at different current density in 0.5 M KI–1 M H₂SO₄ electrolytes; (e) Cycling stability of PANI/MnO₂ using galvanostatic charge discharge measurements at a 2 A/g in 0.5 M KI–1 M H₂SO₄ electrolytes. The inset shows the Nyquist plot of PANI/MnO₂ electrodes before and after cycling stability test.

Figure 8e illustrates the variation of specific capacitance measured at 2 A/g over 500 cycles for PANI/MnO₂. The specific capacitance decreases slightly in the initial 200 cycles and then remains nearly stable. The PANI/MnO₂ shows a loss of the discharge capacity after 500 cycles. The decrease of the specific capacitance may be the result of two things: the structure of the active material has changed due to the charge and discharge repeatedly, caused the enhancement of polarization effect [62,78]; or the I[−] produced I₃[−] and I₅[−] initially, which will decrease the ionic concentration, thus leading to the drop of electrical conductivity. Additionally, there is a noticeable widening of the charge transfer resistance after 500 cycles. In the inset of Figure 8e, the value increased from 0.4 to 1.2 Ω cm² and the electrolyte resistance also increased slightly. These provided firm evidence to the further decrease of specific capacitance [16]. However, it also remains 90% of the specific capacitance, revealing a good cyclic stability.

Table 2. The specific capacitance, electrolyte resistance and charge-transfer resistance at different KI concentration.

KI concentration	C (F/g)	R_s (Ω cm ²)	R_{ct} (Ω cm ²)
1 mol/L	1374	2.07	0.7
0.5 mol/L	1580	1.83	0.4
0.2 mol/L	1405	1.91	0.58
0.1 mol/L	1010	2.3	0.9
0.05 mol/L	571	2.5	1.03

**Figure 9.** Equivalent circuit for PANI/MnO₂ at different concentrations of KI with 1 M H₂SO₄ electrolytes.

4. Conclusions

In summary, the PANI/mesoporous MnO₂ composites have been synthesized successfully by a one-step method. The PANI is well attached to the mesoporous MnO₂ and the specific capacitance of composites and MnO₂ are 1405 and 158 F/g, respectively; the values could be, approximately, a multiple of ten. The introducing of KI enabled us to obtain high specific capacitance of PANI/MnO₂ composite, which can achieve the maximum 1580 F/g at 0.5 mol/L KI. In previous work of other researchers, no others can exceed this value. We also find that the specific capacitance gets larger with the I[−] concentration before 0.5 mol/L, while it begins to decrease beyond that concentration. The constant charge–discharge test was performed at 2, 1, and 0.5 A/g. Even though the specific capacitance decreases with the increasing of current density, the PANI/mesoporous MnO₂ composites present a high ratio discharge property at the current density of 2 A/g; the specific capacitance still attains 857 F/g. In addition, it also exhibits excellent cyclic stability that it remains 90% of the original specific capacitance.

Supplementary Materials: Supplementary materials can be accessed at: <http://www.mdpi.com/2073-4360/7/10/1491/s1>. Figure S1 presents the N₂ adsorption/desorption isotherms and pore size distribution curves of MnO₂. Figure S2 exhibits the Raman spectroscopy of PANI, MnO₂ and PANI/MnO₂.

Acknowledgments: The authors would like to acknowledge the support of the National Natural Science Foundation of China (NSFC, Nos. 21271031, 51573021, 51063009 and 51203012), the Beijing Natural Science Foundation of China (Nos. 2092013, 2132009 and 2122015), the State Key Laboratory of Organic-Inorganic Composites, and the Beijing Municipal Commission of Education for the project on the promotion of innovation in Beijing universities, 2015.

Author Contributions: Xiuguo Cui and Zhongkai Hu conceived and designed the experiments; Zhongkai Hu, Lei Zu, Huiqin Lian, Yanhua Jiang, Yang Liu, Zhenzi Li performed the experiments and analyzed the data; Fei Chen, Xiuguo Cui contributed the analysis tools; Zhongkai Hu wrote the paper.

Conflicts of Interest: The authors declare no conflict of interest.

References

- Ma, L.; Shen, X.; Zhou, H.; Ji, Z.; Chen, K.; Zhu, G. High performance supercapacitor electrode materials based on porous NiCo₂O₄ hexagonal nanoplates/reduced graphene oxide composites. *Chem. Eng. J.* **2015**, *262*, 980–988. [CrossRef]

2. Yuan, C.; Lin, H.; Lu, H.; Xing, E.; Zhang, Y.; Xie, B. Anodic deposition and capacitive property of nano-WO₃·H₂O/MnO₂ composite as supercapacitor electrode material. *Mater. Lett.* **2015**, *148*, 167–170. [[CrossRef](#)]
3. Zhao, Y.; Jiang, P. MnO₂ nanosheets grown on the ZnO-nanorod-modified carbon fibers for supercapacitor electrode materials. *Colloid Surf. A* **2014**, *444*, 232–239. [[CrossRef](#)]
4. Raj, A.T.; Ramanujan, K.; Thangavel, S.; Gopalakrishnan, S.; Raghavan, N.; Venugopal, G. Facile synthesis of vanadium-pentoxide nanoparticles and study on their electrochemical, photocatalytic properties. *J. Nanosci. Nanotechnol.* **2015**, *15*, 3802–3808. [[CrossRef](#)]
5. Gu, H.; Guo, J.; Yan, X.; Wei, H.; Zhang, X.; Liu, J.; Huang, Y.; Wei, S.; Guo, Z. Electrical transport and magnetoresistance in advanced polyaniline nanostructures and nanocomposites. *Polymer* **2014**, *55*, 4405–4419. [[CrossRef](#)]
6. Guo, S.; Lu, G.; Qiu, S.; Liu, J.; Wang, X.; He, C.; Wei, H.; Yan, X.; Guo, Z. Carbon-coated MnO microparticulate porous nanocomposites serving as anode materials with enhanced electrochemical performances. *Nano Energy* **2014**, *9*, 41–49. [[CrossRef](#)]
7. Lv, P.; Feng, Y.Y.; Li, Y.; Feng, W. Carbon fabric-aligned carbon nanotube/MnO₂/conducting polymers ternary composite electrodes with high utilization and mass loading of MnO₂ for super-capacitors. *J. Power Sources* **2012**, *220*, 160–168. [[CrossRef](#)]
8. Chen, W.; Xia, C.; Alshareef, H.N. Graphene based integrated tandem supercapacitors fabricated directly on separators. *Nano Energy* **2015**, *15*, 1–8. [[CrossRef](#)]
9. Khosrozadeh, A.; Xing, M.; Wang, Q. A high-capacitance solid-state supercapacitor based on free-standing film of polyaniline and carbon particles. *Appl. Energy* **2015**, *153*, 87–93. [[CrossRef](#)]
10. Wang, J.-G.; Kang, F.; Wei, B. Engineering of MnO₂-based nanocomposites for high-performance supercapacitors. *Prog. Mater. Sci.* **2015**, *74*, 51–124. [[CrossRef](#)]
11. Mendoza-Sánchez, B.; Coelho, J.; Pokle, A.; Nicolosi, V. A 2D graphene-manganese oxide nanosheet hybrid synthesized by a single step liquid-phase co-exfoliation method for supercapacitor applications. *Electrochim. Acta* **2015**, *174*, 696–705. [[CrossRef](#)]
12. Rose, A.; Raghavan, N.; Thangavel, S.; Uma Maheswari, B.; Nair, D.P.; Venugopal, G. Investigation of cyclic voltammetry of graphene oxide/polyaniline/polyvinylidene fluoride nanofibers prepared via electrospinning. *Mater. Sci. Semicond. Process.* **2015**, *31*, 281–286. [[CrossRef](#)]
13. Park, H.-S.; Lee, M.-H.; Hwang, R.Y.; Park, O.-K.; Jo, K.; Lee, T.; Kim, B.-S.; Song, H.-K. Kinetically enhanced pseudocapacitance of conducting polymer doped with reduced graphene oxide through a miscible electron transfer interface. *Nano Energy* **2014**, *3*, 1–9. [[CrossRef](#)]
14. Sopčić, S.; Roković, M.K.; Mandić, Z.; Róka, A.; Inzelt, G. Mass changes accompanying the pseudocapacitance of hydrous RuO₂ under different experimental conditions. *Electrochim. Acta* **2011**, *56*, 3543–3548. [[CrossRef](#)]
15. Yin, Z.; Zhang, S.; Chen, Y.; Gao, P.; Zhu, C.; Yang, P.; Qi, L. Hierarchical nanosheet-based NiMoO₄ nanotubes: Synthesis and high supercapacitor performance. *J. Mater. Chem. A* **2015**, *3*, 739–745. [[CrossRef](#)]
16. Veerasubramani, G.K.; Krishnamoorthy, K.; Radhakrishnan, S.; Kim, N.-J.; Kim, S.J. Synthesis, characterization, and electrochemical properties of CoMoO₄ nanostructures. *Int. J. Hydrog. Energy* **2014**, *39*, 5186–5193. [[CrossRef](#)]
17. Krishnamoorthy, K.; Veerasubramani, G.K.; Radhakrishnan, S.; Kim, S.J. One pot hydrothermal growth of hierarchical nanostructured Ni₃S₂ on Ni foam for supercapacitor application. *Chem. Eng. J.* **2014**, *251*, 116–122. [[CrossRef](#)]
18. Ghosh, D.; Das, C.K. Hydrothermal growth of hierarchical Ni₃S₂ and Co₃S₄ on a reduced graphene oxide hydrogel@Ni foam: A high-energy-density aqueous asymmetric supercapacitor. *ACS Appl. Mater. Interfaces* **2015**, *7*, 1122–1131. [[CrossRef](#)] [[PubMed](#)]
19. Yang, C.; Wei, H.; Guan, L.; Guo, J.; Wang, Y.; Yan, X.; Zhang, X.; Wei, S.; Guo, Z. Polymer nanocomposites for energy storage, energy saving, and anticorrosion. *J. Mater. Chem. A* **2015**, *3*, 14929–14941. [[CrossRef](#)]
20. Wei, H.; Yan, X.; Wu, S.; Luo, Z.; Wei, S.; Guo, Z. Electropolymerized polyaniline stabilized tungsten oxide nanocomposite films: Electrochromic behavior and electrochemical energy storage. *J. Phys. Chem. C* **2012**, *116*, 25052–25064. [[CrossRef](#)]
21. Zhu, Y.G.; Wang, Y.; Shi, Y.; Wong, J.I.; Yang, H.Y. CoO nanoflowers woven by CNT network for high energy density flexible micro-supercapacitor. *Nano Energy* **2014**, *3*, 46–54. [[CrossRef](#)]

22. Liang, J.; Tan, H.; Xiao, C.; Zhou, G.; Guo, S.; Ding, S. Hydroxyl-riched halloysite clay nanotubes serving as substrate of NiO nanosheets for high-performance supercapacitor. *J. Power Source* **2015**, *285*, 210–216. [[CrossRef](#)]
23. Dinh, T.M.; Achour, A.; Vizireanu, S.; Dinescu, G.; Nistor, L.; Armstrong, K.; Guay, D.; Pech, D. Hydrous RuO₂/carbon nanowalls hierarchical structures for all-solid-state ultrahigh-energy-density micro-supercapacitors. *Nano Energy* **2014**, *10*, 288–294. [[CrossRef](#)]
24. Nair, D.P.; Sakthivel, T.; Nivea, R.; Eshow, J.S.; Gunasekaran, V. Effect of surfactants on electrochemical properties of vanadium-pentoxide nanoparticles synthesized via hydrothermal method. *J. Nanosci. Nanotechnol.* **2015**, *15*, 4392–4397. [[CrossRef](#)] [[PubMed](#)]
25. Liu, W.; Lu, C.; Wang, X.; Tay, R.Y.; Tay, B.K. High-performance microsupercapacitors based on two-dimensional graphene/manganese dioxide/silver nanowire ternary hybrid film. *ACS Nano* **2015**, *9*, 1528–1542. [[CrossRef](#)] [[PubMed](#)]
26. Higgins, T.M.; McAteer, D.; Coelho, J.C.M.; Sanchez, B.M.; Gholamvand, Z.; Moriarty, G.; McEvoy, N.; Berner, N.C.; Duesberg, G.S.; Nicolosi, V.; *et al.* Effect of percolation on the capacitance of supercapacitor electrodes prepared from composites of manganese dioxide nanoplatelets and carbon nanotubes. *ACS Nano* **2014**, *8*, 9567–9579. [[CrossRef](#)]
27. Wei, H.; He, C.; Liu, J.; Gu, H.; Wang, Y.; Yan, X.; Guo, J.; Ding, D.; Shen, N.Z.; Wang, X.; *et al.* Electropolymerized polypyrrole nanocomposites with cobalt oxide coated on carbon paper for electrochemical energy storage. *Polymer* **2015**, *67*, 192–199. [[CrossRef](#)]
28. Zhao, Y.; Wei, H.; Arowo, M.; Yan, X.; Wu, W.; Chen, J.; Wang, Y.; Guo, Z. Electrochemical energy storage by polyaniline nanofibers: high gravity assisted oxidative polymerization *vs.* rapid mixing chemical oxidative polymerization. *Phys. Chem. Chem. Phys.* **2015**, *17*, 1498–1502. [[CrossRef](#)] [[PubMed](#)]
29. Wei, H.; Wang, Y.; Guo, J.; Yan, X.; O'Connor, R.; Zhang, X.; Shen, N.Z.; Weeks, B.L.; Huang, X.; Wei, S.; *et al.* Electropolymerized polypyrrole nanocoatings on carbon paper for electrochemical energy storage. *ChemElectroChem* **2015**, *2*, 119–126. [[CrossRef](#)]
30. Grover, S.; Goel, S.; Sahu, V.; Singh, G.; Sharma, R.K. Asymmetric supercapacitive characteristics of pani embedded holey graphene nanoribbons. *ACS Sustain. Chem. Eng.* **2015**, *3*, 1460–1469. [[CrossRef](#)]
31. Lu, X.-F.; Chen, X.-Y.; Zhou, W.; Tong, Y.-X.; Li, G.-R. α -Fe₂O₃@PANI core-shell nanowire arrays as negative electrodes for asymmetric supercapacitors. *ACS Appl. Mater. Interface* **2015**, *7*, 14843–14850. [[CrossRef](#)] [[PubMed](#)]
32. Wei, H.; Gu, H.; Guo, J.; Wei, S.; Guo, Z. Electropolymerized polyaniline nanocomposites from multi-walled carbon nanotubes with tuned surface functionalities for electrochemical energy storage. *J. Electrochem. Soc.* **2013**, *160*, G3038–G3045. [[CrossRef](#)]
33. Zhao, Y.; Ran, W.; He, J.; Huang, Y.; Liu, Z.; Liu, W.; Tang, Y.; Zhang, L.; Gao, D.; Gao, F. High-performance asymmetric supercapacitors based on multilayer MnO₂/graphene oxide nanoflakes and hierarchical porous carbon with enhanced cycling stability. *Small* **2015**, *11*, 1310–1319. [[CrossRef](#)] [[PubMed](#)]
34. Sun, L.-J.; Liu, X.-X. Electrodepositions and capacitive properties of hybrid films of polyaniline and manganese dioxide with fibrous morphologies. *Eur. Polym. J.* **2008**, *44*, 219–224. [[CrossRef](#)]
35. Chen, L.; Sun, L.-J.; Luan, F.; Liang, Y.; Li, Y.; Liu, X.-X. Synthesis and pseudocapacitive studies of composite films of polyaniline and manganese oxide nanoparticles. *J. Power Source* **2010**, *195*, 3742–3747. [[CrossRef](#)]
36. Kim, J.; Ju, H.; Inamdar, A.I.; Jo, Y.; Han, J.; Kim, H.; Im, H. Synthesis and enhanced electrochemical supercapacitor properties of Ag–MnO₂–polyaniline nanocomposite electrodes. *Energy* **2014**, *70*, 473–477. [[CrossRef](#)]
37. Chen, L.; Song, Z.; Liu, G.; Qiu, J.; Yu, C.; Qin, J.; Ma, L.; Tian, F.; Liu, W. Synthesis and electrochemical performance of polyaniline–MnO₂ nanowire composites for supercapacitors. *J. Phys. Chem. Solids* **2013**, *74*, 360–365. [[CrossRef](#)]
38. Li, Q.; Liu, J.; Zou, J.; Chunder, A.; Chen, Y.; Zhai, L. Synthesis and electrochemical performance of multi-walled carbon nanotube/polyaniline/MnO₂ ternary coaxial nanostructures for supercapacitors. *J. Power Source* **2011**, *196*, 565–572. [[CrossRef](#)]
39. Wang, J.-G.; Yang, Y.; Huang, Z.-H.; Kang, F. Interfacial synthesis of mesoporous MnO₂/polyaniline hollow spheres and their application in electrochemical capacitors. *J. Power Sources* **2012**, *204*, 236–243. [[CrossRef](#)]

40. Su, L.-H.; Zhang, X.-G.; Mi, C.-H.; Gao, B.; Liu, Y. Improvement of the capacitive performances for Co–Al layered double hydroxide by adding hexacyanoferrate into the electrolyte. *Phys. Chem. Chem. Phys.* **2009**, *11*, 2195–2202. [[CrossRef](#)] [[PubMed](#)]
41. Li, Q.; Li, K.; Sun, C.; Li, Y. An investigation of Cu²⁺ and Fe²⁺ ions as active materials for electrochemical redox supercapacitors. *J. Electroanal. Chem.* **2007**, *611*, 43–50. [[CrossRef](#)]
42. Lota, G.; Frackowiak, E. Striking capacitance of carbon/iodide interface. *Electrochem. Commun.* **2009**, *11*, 87–90. [[CrossRef](#)]
43. Senthilkumar, S.T.; Selvan, R.K.; Ponpandian, N.; Melo, J.S.; Lee, Y.S. Improved performance of electric double layer capacitor using redox additive (VO²⁺/VO²⁺) aqueous electrolyte. *J. Mater. Chem. A* **2013**, *1*, 7913–7919. [[CrossRef](#)]
44. Senthilkumar, S.T.; Selvan, R.K.; Melo, J.S. Redox additive/active electrolytes: A novel approach to enhance the performance of supercapacitors. *J. Mater. Chem. A* **2013**, *1*, 12386–12394. [[CrossRef](#)]
45. Stejskal, J.; Trchová, M.; Blinova, N.V.; Konyushenko, E.N.; Reynaud, S.; Prokeš, J. The reaction of polyaniline with iodine. *Polymer* **2008**, *49*, 180–185. [[CrossRef](#)]
46. Adhikari, S.; Banerji, P. Enhanced conductivity in iodine doped polyaniline thin film formed by thermal evaporation. *Thin Solid Films* **2010**, *518*, 5421–5425. [[CrossRef](#)]
47. Stejskal, J.; Sapurina, I.; Trchová, M. Polyaniline nanostructures and the role of aniline oligomers in their formation. *Prog. Polym. Sci.* **2010**, *35*, 1420–1481. [[CrossRef](#)]
48. Wang, S.-G.; Gong, W.-X.; Liu, X.-W.; Yao, Y.-W.; Gao, B.-Y.; Yue, Q.-Y. Removal of lead(II) from aqueous solution by adsorption onto manganese oxide-coated carbon nanotubes. *Sep. Purif. Technol.* **2007**, *58*, 17–23. [[CrossRef](#)]
49. Zhang, H.; Xu, M.; Wang, H.-J.; Lei, D.; Qu, D.; Zhai, Y.-J. Adsorption of copper by aminopropyl functionalized mesoporous delta manganese dioxide from aqueous solution. *Colloid Surf. A* **2013**, *435*, 78–84. [[CrossRef](#)]
50. Bian, C.; Yu, A. De-doped polyaniline nanofibres with micropores for high-rate aqueous electrochemical capacitor. *Synth. Metal* **2010**, *160*, 1579–1583. [[CrossRef](#)]
51. Yang, X.-F.; Wang, G.-C.; Wang, R.-Y.; Li, X.-W. A novel layered manganese oxide/poly (aniline-co-o-anisidine) nanocomposite and its application for electrochemical supercapacitor. *Electrochim. Acta* **2010**, *55*, 5414–5419. [[CrossRef](#)]
52. Zhu, Y.; Hu, D.; Wan, M.X.; Jiang, L.; Wei, Y. Conducting and superhydrophobic rambutan-like hollow spheres of polyaniline. *Adv. Mater.* **2007**, *19*, 2092–2096. [[CrossRef](#)]
53. Wang, Y.-T.; Lu, A.-H.; Li, W.-C. Mesoporous manganese dioxide prepared under acidic conditions as high performance electrode material for hybrid supercapacitors. *Microporous Mesoporous Mater.* **2012**, *153*, 247–253. [[CrossRef](#)]
54. Zhang, J.; Shu, D.; Zhang, T.; Chen, H.; Zhao, H.; Wang, Y.; Sun, Z.; Tang, S.; Fang, X.; Cao, X. Capacitive properties of PANI/MnO₂ synthesized via simultaneous-oxidation route. *J. Alloys Compd.* **2012**, *532*, 1–9. [[CrossRef](#)]
55. Gu, H.; Huang, Y.; Zhang, X.; Wang, Q.; Zhu, J.; Shao, L.; Haldolaarachchige, N.; Young, D.P.; Wei, S.; Guo, Z. Magneto-resistive polyaniline-magnetite nanocomposites with negative dielectrical properties. *Polymer* **2012**, *53*, 801–809. [[CrossRef](#)]
56. Zhang, X.; Zhu, J.; Haldolaarachchige, N.; Ryu, J.; Young, D.P.; Wei, S.; Guo, Z. Synthetic process engineered polyaniline nanostructures with tunable morphology and physical properties. *Polymer* **2012**, *53*, 2109–2120. [[CrossRef](#)]
57. Vahlman, H.; Halme, J.; Korhonen, J.; Aitola, K.; Patakangas, J. On the mass transport in apparently iodine-free ionic liquid polyaniline-coated carbon black composite electrolytes in dye-sensitized solar cells. *J. Phys. Chem. C* **2013**, *117*, 11920–11929. [[CrossRef](#)]
58. Lee, Y.W.; Do, K.; Lee, T.H.; Jeon, S.S.; Yoon, W.J.; Kim, C.; Ko, J.; Im, S.S. Iodine vapor doped polyaniline nanoparticles counter electrodes for dye-sensitized solar cells. *Synth. Metals* **2013**, *174*, 6–13. [[CrossRef](#)]
59. Ayad, M.M.; Amer, W.A.; Stejskal, J. Effect of iodine solutions on polyaniline films. *Thin Solid Films* **2009**, *517*, 5969–5973. [[CrossRef](#)]
60. Barman, T.; Pal, A.R. Contradictory ageing behaviour and optical property of iodine doped and H₂SO₄ doped pulsed DC plasma polymerized aniline thin films. *Solid State Sci.* **2013**, *24*, 71–78. [[CrossRef](#)]

61. Yelil Arasi, A.; Juliet Latha Jeyakumari, J.; Sundaresan, B.; Dhanalakshmi, V.; Anbarasan, R. The structural properties of Poly(aniline)—Analysis via FTIR spectroscopy. *Spectrochim. Acta Part A* **2009**, *74*, 1229–1234. [[CrossRef](#)] [[PubMed](#)]
62. Wei, H.; Gu, H.; Guo, J.; Wei, S.; Liu, J.; Guo, Z. Silica doped polyaniline with endured electrochemical energy storage and the magnetic field effects. *J. Phys. Chem. C* **2013**, *117*, 13000–13010.
63. Zhang, Y.; Mo, Y. Preparation of MnO₂ electrodes coated by Sb-doped SnO₂ and their effect on electrochemical performance for supercapacitor. *Electrochim. Acta* **2014**, *142*, 76–83. [[CrossRef](#)]
64. Zeng, X.-R.; Ko, T.-M. Structures and properties of chemically reduced polyanilines. *Polymer* **1998**, *39*, 1187–1195. [[CrossRef](#)]
65. Yu, L.; Gan, M.; Ma, L.; Huang, H.; Hu, H.; Li, Y.; Tu, Y.; Ge, C.; Yang, F.; Yan, J. Facile synthesis of MnO₂/polyaniline nanorod arrays based on graphene and its electrochemical performance. *Synth. Metals* **2014**, *198*, 167–174. [[CrossRef](#)]
66. Zhang, X.; Ji, L.; Zhang, S.; Yang, W. Synthesis of a novel polyaniline-intercalated layered manganese oxide nanocomposite as electrode material for electrochemical capacitor. *J. Power Source* **2007**, *173*, 1017–1023. [[CrossRef](#)]
67. Liu, F.-J.; Hsu, T.-F.; Yang, C.-H. Construction of composite electrodes comprising manganese dioxide nanoparticles distributed in polyaniline–poly(4-styrene sulfonic acid-co-maleic acid) for electrochemical supercapacitor. *J. Power Source* **2009**, *191*, 678–683. [[CrossRef](#)]
68. Sun, L.-J.; Liu, X.-X.; Lau, K.K.-T.; Chen, L.; Gu, W.-M. Electrodeposited hybrid films of polyaniline and manganese oxide in nanofibrous structures for electrochemical supercapacitor. *Electrochim. Acta* **2008**, *53*, 3036–3042. [[CrossRef](#)]
69. Prasad, K.R.; Miura, N. Polyaniline-MnO₂ composite electrode for high energy density electrochemical capacitor. *Electrochem. Solid State Lett.* **2004**, *7*, A425–A428. [[CrossRef](#)]
70. Zhou, Z.; Cai, N.; Zhou, Y. Capacitive characteristics of manganese oxides and polyaniline composite thin film deposited on porous carbon. *Mater. Chem. Phys.* **2005**, *94*, 371–375. [[CrossRef](#)]
71. Yuan, C.; Su, L.; Gao, B.; Zhang, X. Enhanced electrochemical stability and charge storage of MnO₂/carbon nanotubes composite modified by polyaniline coating layer in acidic electrolytes. *Electrochim. Acta* **2008**, *53*, 7039–7047. [[CrossRef](#)]
72. Kim, K.-S.; Park, S.-J. Synthesis and high electrochemical performance of polyaniline/MnO₂-coated multi-walled carbon nanotube-based hybrid electrodes. *J. Solid State Electrochem.* **2012**, *16*, 2751–2758. [[CrossRef](#)]
73. Meng, F.; Yan, X.; Zhu, Y.; Si, P. Controllable synthesis of MnO₂/polyaniline nanocomposite and its electrochemical capacitive property. *Nanoscale Res. Lett.* **2013**, *8*, 1–8. [[CrossRef](#)] [[PubMed](#)]
74. Jaidev; Jafri, R.I.; Mishra, A.K.; Ramaprabhu, S. Polyaniline-MnO₂ nanotube hybrid nanocomposite as supercapacitor electrode material in acidic electrolyte. *J. Mater. Chem.* **2011**, *21*, 17601–17605. [[CrossRef](#)]
75. Dissanayake, M.A.K.L.; Rupasinghe, W.N.S.; Seneviratne, V.A.; Thotawatthage, C.A.; Senadeera, G.K.R. Optimization of iodide ion conductivity and nano filler effect for efficiency enhancement in polyethylene oxide (PEO) based dye sensitized solar cells. *Electrochim. Acta* **2014**, *145*, 319–326. [[CrossRef](#)]
76. Rawal, R.; Chawla, S.; Malik, P.; Pundir, C.S. An amperometric biosensor based on laccase immobilized onto MnO₂NPs/cMWCNT/PANI modified Au electrode. *Int. J. Biol. Macromol.* **2012**, *51*, 175–181. [[CrossRef](#)] [[PubMed](#)]
77. Yu, H.; Wu, J.; Fan, L.; Xu, K.; Zhong, X.; Lin, Y.; Lin, J. Improvement of the performance for quasi-solid-state supercapacitor by using PVA–KOH–KI polymer gel electrolyte. *Electrochim. Acta* **2011**, *56*, 6881–6886. [[CrossRef](#)]
78. Wei, H.; Zhu, J.; Wu, S.; Wei, S.; Guo, Z. Electrochromic polyaniline/graphite oxide nanocomposites with endured electrochemical energy storage. *Polymer* **2013**, *54*, 1820–1831. [[CrossRef](#)]

